Materials Science & Engineering A 802 (2021) 140653

Contents lists available at ScienceDirect

Materials Science & Engineering A

journal homepage: http://www.elsevier.com/locate/msea

An examination of microstructural evolution in a Pb–Sn eutectic alloy processed by high-pressure torsion and subsequent self-annealing

Nian Xian Zhang [a,b], Megumi Kawasaki [c], Yi Huang [a,d,*], Terence G. Langdon [a,e]

[a] Materials Research Group, Department of Mechanical Engineering, University of Southampton, Southampton, SO17 1BJ, UK
[b] Materials Department, Crown Technology, Downsview Road, Wantage, OX12 9BP, UK
[c] School of Mechanical, Industrial and Manufacturing Engineering, Oregon State University, Corvallis, OR, 97331, USA
[d] Department of Design and Engineering, Faculty of Science and Technology, Bournemouth University, Poole, Dorset BH12 5BB, UK
[e] Departments of Aerospace, Mechanical Engineering and Materials Science, University of Southern California, Los Angeles, CA, 90089-1453, USA

ARTICLE INFO

Keywords:
High-pressure torsion
Pb–Sn alloy
Self-annealing
Solubility
Twin boundaries

ABSTRACT

The Pb–Sn alloy has a wide use in the electronic, energy storage and nuclear industries and a fine-grained Pb–Sn alloy may open up new possibilities for applications in these industries. In order to understand the behavior of grain refinement, a Pb-62% Sn eutectic alloy was processed by high-pressure torsion (HPT), stored at room temperature (RT) and then the microstructures of the alloy after HPT were repeatedly investigated during the course of self-annealing using electron backscatter diffraction, scanning electron microscopy and transmission electron microscopy. It is demonstrated that there is a large fraction of twin boundaries with a twin relationship of 62.8°<100> in the microstructure of the initial as-cast condition. Due to the presence of the high imposed pressure, the mobility of Σ21 boundaries at 71° is greatly favoured during processing by HPT. After the high pressure is removed, the mobility of dislocation-twin boundaries near 62.8°<100> is then favoured. Processing by HPT significantly increases the solubility of Sn in the Pb phase. The supersaturated state of Sn in Pb is not stable during self-annealing at RT and instead a decomposition of Sn from the Pb-rich phase is observed after storage for 16 days. The main mechanism for this decomposition is lattice diffusion.

1. Introduction

The grain size is probably the most important structural parameter in metals because it governs many of the fundamental properties including strength and flow mechanisms. Generally, the grain size may be varied using conventional thermo-mechanical processing but in practice this has a limitation because it is not possible to achieve exceptional grain refinement to produce grain sizes within the submicrometer or the nanometer ranges. An alternative approach was developed more than two decades ago whereby very small grains are produced by subjecting a metal to severe plastic deformation (SPD) in which a high strain is imposed but without incurring any significant change in the overall dimensions of the sample [1]. Numerous SPD processing methods are now available and detailed descriptions of these methods are given elsewhere [2,3]. Nevertheless, the two most attractive SPD procedures are equal-channel angular pressing (ECAP) and high-pressure torsion (HPT) [4,5]. In processing by ECAP, the sample is in the form of a bar or rod and it is pressed through a die constrained within a channel which is bent through a sharp angle, often but not always 90°, near the centre of the die [6]. In processing by HPT, the sample is usually in the form of a thin disk and it is placed between two massive anvils and subjected to a high applied pressure and concurrent torsional straining [7]. In practice, HPT processing has two significant advantages over ECAP because it produces both grains having smaller sizes [8,9] and higher fractions of grain boundaries having high angles of misorientation [10].

The Pb–Sn alloy has been conventionally utilized as a solder material but the alloy has received only limited attention because of the concerns of lead toxicity. Nevertheless, recent research using the Pb–Sn alloy has demonstrated the recycling of valuable Pb and Sn elements from electronic waste and the regeneration of the Pb–Sn alloy using green procedures [11,12]. Recent developments in the applications of the Pb–Sn alloy are also remarkable in the energy sector: for example, a grid-scale Pb-acid battery for energy storage [13,14] and shielding materials for highly penetrating radiations of gamma rays during the reactions occurring in nuclear reactors [15]. The materials used for such energy applications require the development in synthesis and processing of

* Corresponding author. Department of Design and Engineering, Faculty of Science and Technology, Bournemouth University, Poole, Dorset, BH12 5BB, UK.
E-mail address: yhuang2@bournemouth.ac.uk (Y. Huang).

https://doi.org/10.1016/j.msea.2020.140653
Received 4 November 2020; Received in revised form 3 December 2020; Accepted 7 December 2020
Available online 11 December 2020

bulk-scale nanostructured materials and an understanding and improvement of their microstructural stability. In this context, the present fundamental research provides information on the significance of grain refinement in the development of the Pb–Sn alloy for a wide range of applications.

This study was initiated specifically to investigate the microstructural evolution occurring in a Pb-62% Sn (wt. %) eutectic alloy during HPT processing and subsequent self-annealing through storage at room temperature (RT). This alloy is used extensively for soldering in electronic packaging and in the assembly of printed circuit boards [16,17] but it has a low absolute melting temperature, T_m, of only 456 K so that RT corresponds to $\sim 0.65T_m$. Nevertheless, the dual phase structure tends to inhibit grain growth and this provides a potential for achieving good superplastic elongations in tensile testing at room temperature [18–20] and exceptionally high elongations at 413 K of 3060% [21] and 4850% [22].

The Pb-62% Sn alloy consists of a β-Sn phase having a body-centered tetragonal (BCT) crystal structure and a Pb-rich phase that is normally either spheroidal or lamellar in shape depending on the cooling rate during solidification and the heat treatment history. Numerous investigations of the solidification of Pb–Sn solder balls have shown that the Sn-rich phase grows by a dendritic mechanism and the individual Sn dendrites may grow to lengths of up to hundreds of micrometers [23,24]. This is due to undercooling which produces rapid dendritic growth so that only a few Sn grains are formed. In practice, the Sn grains commonly form solidification twins with twinning planes of {101} and {301} having a common direction of <100> and at twin angles of 57.2° and 62.8°, respectively [25,26]. Other special grain boundaries having high fractions were also reported for the deformed microstructures in Sn-based alloys [27]. It should be noted that these observations are based primarily on solder balls which generally have sizes below 1 mm but there is no significant information on the microstructures of bulk Sn alloys and the evolution of microstructures and the formation of special boundaries after processing by HPT. A recent report described elemental and spinodal decompositions in a similar type of two-phase alloy, Al-30 mol% Zn with a low absolute melting temperature, where a nano-sized lamellar structure occurred in the solution-treated sample but this was fragmented by HPT processing leading to a significant loss of strength [28].

It is anticipated that processing by HPT will have a significant effect on the Pb–Sn alloy since RT is above $0.5T_m$ so that dynamic recrystallization (DRX) should be activated. Earlier investigations demonstrated the influence of hydrostatic pressure on grain boundary mobility where the pressure was introduced by atmospheric pressure in a fluid chamber using a pressure control device instead of through the hydrostatic pressure from massive anvils as in HPT and the samples were annealed at elevated temperatures to activate boundary migration in bicrystals of Sn [29] and Al [30]. Evidence was presented earlier that the self-annealing behavior in the Pb–Sn alloy occurs immediately after HPT processing [31] and there are also extensive recent results showing the effect of self-annealing at room temperature on the microstructural characteristics and the mechanical properties of a Bi-42% Sn eutectic alloy processed by HPT [32]. Accordingly, the present investigation provides a comprehensive evaluation of microstructural evolution in the Pb–Sn alloy after HPT processing followed by self-annealing for periods of up to 24 days.

2. Experimental material and procedures

The experiments were performed using a Pb-62% Sn (wt.%) eutectic alloy which was received as an as-cast billet having dimensions of 34 × 20 × 15 mm^3. The initial material contained a binary microstructure with Pb-rich and Sn-rich phases and the mean linear intercept grain size was determined as ~2.5 μm by measuring both phases. Further details of the alloy were given earlier [33].

The alloy was initially machined into discs having thicknesses of ~1.2–1.5 mm and both sides of each disc were then carefully polished to give HPT disc samples having initial thicknesses of ~0.80 mm. The processing by HPT was conducted at RT under quasi-constrained conditions in which there is a small outflow of material around the periphery of the disc during processing [34,35]. Each disc was processed for a total number of revolutions, N, of 1 turn under an applied load of ~24 ton corresponding to an applied compressive pressure of $P = 3.0$ GPa. After HPT processing, the discs were removed from the HPT facility and stored at RT for various periods up to a maximum of 24 days in order to examine the evolution during self-annealing.

The microstructures of the as-cast and the HPT-processed samples were recorded by electron backscatter diffraction (EBSD) using a JSM6500F thermal field emission scanning electron microscope (SEM) equipped with a charge-coupled device (CCD) camera for acquiring electron diffraction patterns. For sample preparation, the discs were subjected to careful grinding and polishing with abrasive papers and diamond paste. All polished discs were etched for ~5 s in a solution of 25 ml H_2O, 5 ml HCl with a concentration of 37% and 5 g of NH_4NO_3 to remove any residual stresses introduced during polishing. Orientation imaging microscopy (OIM) maps and SEM images of the same regions having sizes of 27 × 15 μm^2 located near the edge of the disc were recorded both immediately after the HPT processing and after 2, 7 and 24 days of storage at RT. In order to easily find the same location on the disc for each separate observation, the position was carefully defined by using an embedded dust particle as a reference point. The EBSD patterns were collected using step sizes for the as-cast and HPT-processed samples of 0.3 and 0.15 μm, respectively, and this was followed by a clean-up procedure removing less than 10% of the total points measured. Information on the grain boundary misorientation angles were obtained from OIM maps covering larger scan areas of 45 × 35 μm^2.

Detailed microstructural observations of the as-cast and the HPT specimens stored at RT were obtained by transmission electron microscopy (TEM) using a Cs-corrected JEOL JEM-2100F with an accelerating voltage of 200 kV. All TEM specimens were prepared by an *in situ* lift-out technique using a Klocke Nanotechnik micro-manipulator in a Tescan LYRA 1 focused ion beam (FIB) facility. Since the Pb–Sn alloy is exceptionally soft and has a low melting temperature, it was necessary to perform the FIB milling with extreme care to avoid any extraneous damage such as the falling of the Pb phase from the specimens. An initial rough milling was conducted at 30 kV and 5 nA and this was followed by a final thinning at 5 kV and 50 pA. The chemical compositions of both the Sn-rich and the Pb-rich phases were examined using an Oxford Instruments silicon drift detector (SDD) in energy-dispersive X-ray spectroscopy (EDS) operating in the scanning TEM (STEM) mode. EDS maps were developed with the Pb and Sn assigned different colours.

3. Experimental results

3.1. Microstructure of the as-cast alloy

A typical SEM image of the Pb–Sn alloy in the as-cast condition is shown in Fig. 1(a) where the primary colours of light grey and dark grey correspond to the Pb-rich and the Sn-rich phases, respectively. Most investigations of this alloy generally simplify the microstructure as a mixture of the two phases [18–20] but in practice the microstructure is more complex. Thus, in Fig. 1(a) this inherent complexity becomes apparent by marking additional boundaries by red dashed lines which thereby divide the microstructure into several large domains each having many Sn-rich grains and with the Pb-phase having both equiaxed and lamellar shapes. The existence of these domains was confirmed by performing EBSD to identify the dominant orientation components within each domain, as shown in Fig. 1(b) where the phase map of the same area as in Fig. 1(a) depicts the Pb-rich phase in red and the Sn-rich phase in blue and there is a clear confirmation of the two-phase microstructure.

Fig. 1(c) shows the OIM image of the Sn grains in Fig. 1(a and b) and

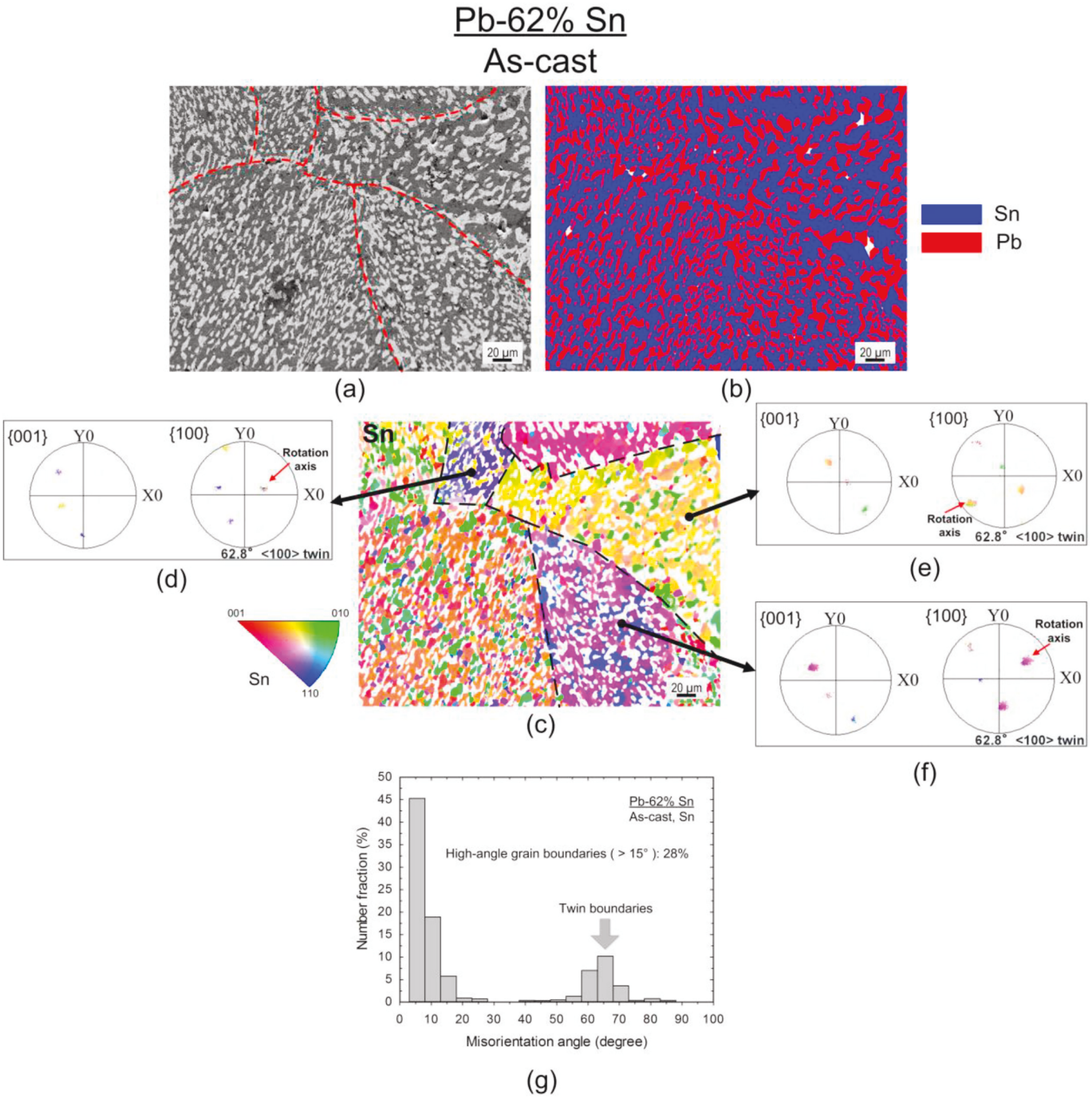

Fig. 1. (a) SEM image, (b) EBSD mapping and (c) OIM image of the Pb–Sn alloy in the as-cast condition, (d), (e) and (f) are the {001} and {100} pole figures of three domains and (g) shows the grain misorientation angles.

it is evident that there are certain combinations of orientations represented by the different colours in each domain so that it is easy to separately identify the different domains. The {001} and {100} pole figures taken at three representative domains separated by the black dashed lines are shown in Fig. 1 (d), (e) and (f), respectively, with the unit triangle shown at lower left. It is confirmed from the {001} pole figures that there are three clusters of dominant orientations within each domain whereas in the {100} pole figures it is clear that for each domain the three orientations rotate with an axis that is at 62.8° with respect to the <100> crystal direction. The reason is because in a {100} map all three colours representing the three orientations have components that overlap where the red arrows are indicated in Fig. 1 (d), (e) and (f) which are rotation axes. These are in twin relationship with a rotation angle of 62.8° around the <100> axis [26]. Fig. 1(g) shows the overall distribution of the grain boundary misorientations of the Sn grains from the OIM map in Fig. 1(c) and the peak misorientation angles from 60° to 65° confirm that most high-angle grain boundaries (HAGBs) are 62.8° <100> twin boundaries. It should be noted also that the fraction of low-angle grain boundaries (LAGBs) is very high (72%).

3.2. *In situ* observations during self-annealing

Representative *in situ* observations during self-annealing are shown in Fig. 2 at the edge of the Pb–Sn disc after processing by HPT for one

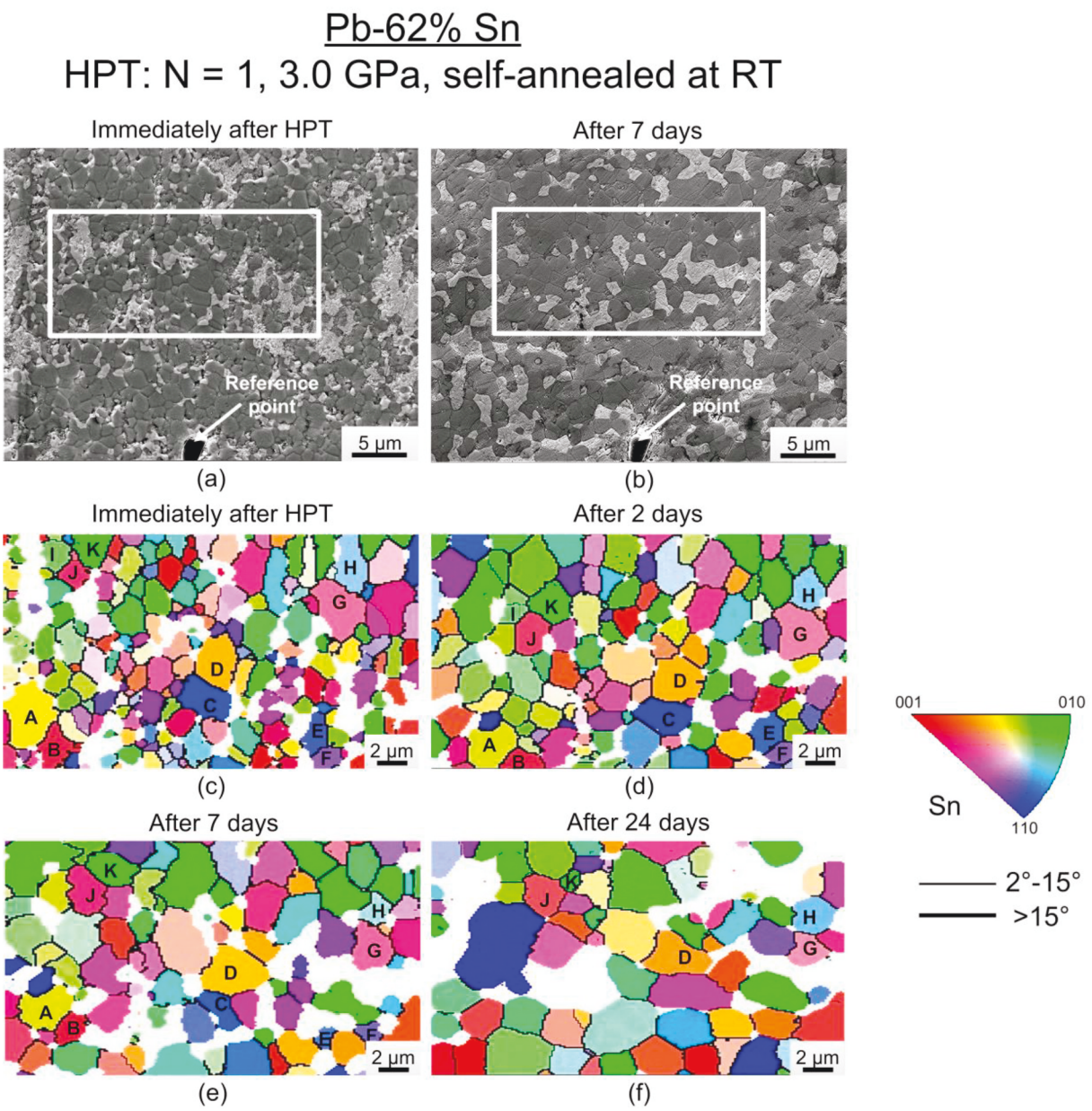

Fig. 2. SEM images and EBSD measurements of the a same location on a sample processed by HPT and stored at RT for up to 24 days: the embedded dust particle was used as a reference point to locate the same position and the large grains are marked by letters from A to K.

turn where Fig. 2(a) and (b) are SEM images immediately after HPT and after 7 days of storage, respectively, where the Sn-rich grains are dark grey and the Pb-rich phase is light grey: an embedded dust particle, which served as a reference point for locating the same position for the SEM and EBSD observations, is indicated by white arrows in Fig. 2(a) and (b). Corresponding OIM images are shown in Fig. 2(c)–(f) for the Sn grains in the area denoted by the white boxes in Fig. 2(a) and (b) corresponding to (c) immediately after HPT processing and after self-annealing at RT for (d) 2, (e) 7 and (f) 24 days, respectively, where the unit triangle is shown on the right.

For convenience, all images from Fig. 2(c)–(f) are at the same magnification and some of the larger Sn grains are marked in Fig. 2(c) with letters from A to K to assist in visualizing and locating the recrystallization sites during the subsequent self-annealing. Several conclusions are reached by careful inspection of Fig. 2(c)–(f). First, the Sn grain size is much finer immediately after HPT processing and thereafter the grain size increases significantly during storage at RT. Second, recrystallization occurs during self-annealing and the nucleation sites are generally located near grain boundaries. Third, the newly-formed grains initially consume the original grains and then move on to consume other close grains. An example of this latter process is visible in Fig. 2(d) and (e) where the blue grain newly-formed above grain A starts to consume grain A in Fig. 2(d) and then also consumes the adjacent grain B in Fig. 2 (f). Finally, the Pb-rich phase is broken into fine particles by the HPT processing and thereafter rejoins with nearby particles and increases in size as self-annealing proceeds.

For additional observations on the precise nature of the recrystallization process, two newly-formed grains marked A′ and C′, nucleated in the vicinity of grains A and C in Fig. 2(c)–(f), respectively, are shown with their neighboring grains in Fig. 3(a) and (b) immediately after HPT and after self-annealing for various periods up to 24 days. The {100} pole figures for A′ and C′ and the original grains of A and C are given on the right of Fig. 3. From these pole figures it is evident that the newly-formed grains and the original grains have a near twin relationship although the rotation axes slightly deviate from the 62.8° <100> twinning axis by 1.6° and 1.1° in Fig. 3(a) and (b), respectively.

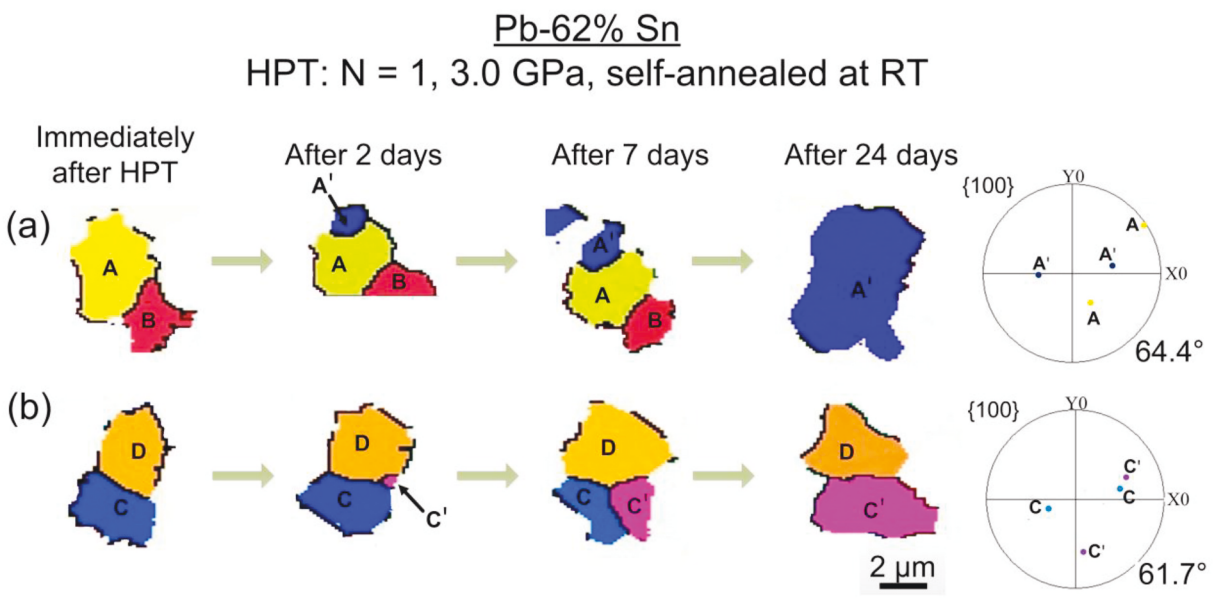

Fig. 3. (a) and (b) show images of two different sets of newly-recrystallized grains and the original grains obtained from Fig. 2 together with their {100} pole figures.

Fig. 4(a) and (b) shows the grain boundary misorientations for the Sn grains as obtained from the EBSD measurements immediately after HPT processing and after 11 days of storage at RT, respectively. It is readily apparent that there are significant increases in the fractions of HAGBs after HPT in Fig. 4 compared with the initial as-cast condition in Fig. 1 (g). The measurement of the fraction of HAGBs immediately after HPT is exceptionally high at 98% but the fraction of LAGBs gradually increases as the alloy is stored and self-annealed at RT while most of the HAGBs are distributed within the range from 55° to 75°.

The common special boundaries for Sn-based alloys are summarized in Table 1 [29,36]. Therefore, it is concluded from inspection of Table 1 that the observed high fractions of misorientation angles at 60–70° for the Sn grains immediately after HPT processing and after HPT and self-annealing in Fig. 4(a) and (b) include large numbers of twin boundaries at 62.8° and Σ21 boundaries at 71°. In order to clarify the nature of the peaks for the HAGBs in the as-cast sample and in the HPT-processed samples with different self-annealing times from 0 to 11 days at RT, the distributions of the misorientation angles are shown in Fig. 5 using a small range of high angles from 55° to 75°. Thus, there is a

Table 1
Commonly observed special boundaries in Sn alloys [30,36].

Angle	22.5°	28°	37°	57.2°	62.8°	71°
CSL Σ	13	17	5	Twin	Twin	21

tendency for peak shifting during processing and storage in terms of both the position and intensity of the peaks and this leads to four separate conclusions. First, for the initial as-cast sample the major peak is located close to 62.8° which is defined as a twin angle in Table 1 and there is also a small peak close to 69° which probably corresponds to Σ21 boundaries. Second, immediately after HPT processing, as shown by the data marked 0 day, the fraction at ~69° increases significantly but there is no apparent peak for twin boundaries at 62.8°. Third, the peaks at ~69° gradually decrease with increasing self-annealing time for the HPT-processed samples while the fractions of twin boundaries at ~62.8° gradually increase. Fourth, there is a deviation for the peak of the twin boundaries at 62.8° during longer-term storage after HPT and this is in

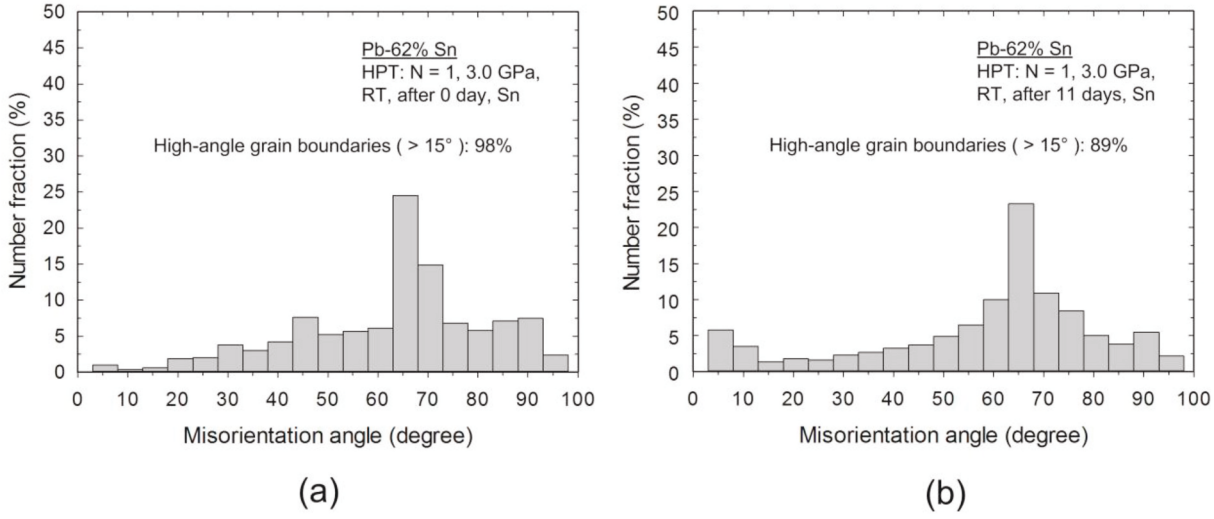

Fig. 4. Number fraction as a percentage plotted against the misorientation angle of Sn grains for a sample (a) immediately after processing by HPT and (b) after storing at RT for 11 days.

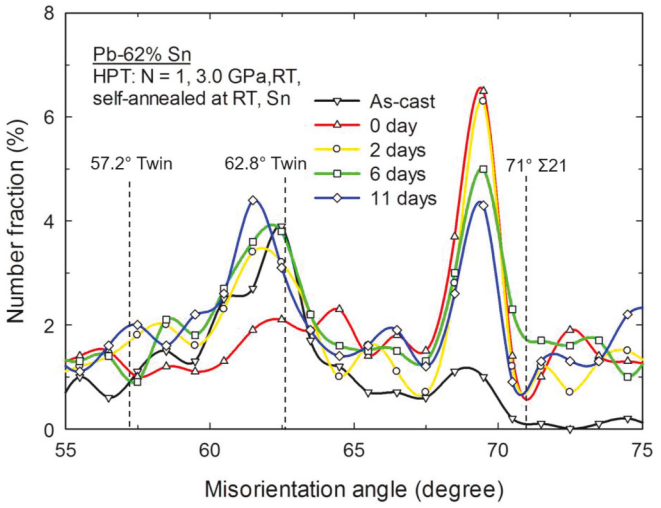

Fig. 5. Number fractions as a percentage plotted against the misorientation angle over the range from 55° to 75° for the as-cast sample, an HPT-processed sample after 0 days (immediately after HPT), and after storage at RT for 2, 6 and 11 days. Dashed lines indicate special boundaries in Table 1 including 57.2° and 62.8° twin and Σ21 at 71°.

excellent agreement with the {100} pole figures in Fig. 3 where the rotation axes of the recrystallized grains deviate from 62.8° for the original grain.

3.3. Microstructural features of the Pb phase

Fig. 6 shows SEM images taken from thin slices of the Pb–Sn samples separated by FIB in (a) an as-cast condition and in the HPT-processed condition after storage at RT for (b) 3 and (c) 16 days: gaps are shown in black colour between the Pb and Sn phases and these gaps are especially apparent in Fig. 6(b) where they correspond to clearly-defined micro-holes at places where Pb-rich phases were accidently removed during the FIB operation. This removal confirms that the bonding between the Sn-rich and the Pb-rich phase is very weak. Additionally, the Pb-rich phase has both lamellar and equiaxed configurations in the as-cast condition as marked in Fig. 6(a) but there are no visible lamellar Pb-rich phases after HPT. The average size of the Pb-rich phase is reduced significantly by HPT after 3 days of storage in Fig. 6(b) and then grows back to larger particles after 16 days of storage.

It is interesting to note that a similar evolution in a duplex microstructure from a lamellar structure to a structure of fine equiaxed grains was observed earlier in a Zn-22% Al eutectoid alloy having low T_m when processing by HPT at room temperature up to 4 turns under a pressure of 6.0 GPa [37,38]. The observed very fine equiaxed grains of Zn and Al immediately after HPT were newly formed by the breaking of lamellae and all of the refined microstructure experienced dynamic equilibrium in the later stages of dynamic recrystallization in the highly strained regions to give a relatively uniform and equiaxed UFG structure [39].

Considering the area within the black box shown at the upper left in Fig. 6(c), closer views of the Pb-rich phases are given in Fig. 7 where, as indicated by the upper labels, there are TEM images, EDS maps and HRTEM images for the samples in the as-cast condition and after HPT for 1 turn and storage at RT for 3 days shown by two different areas and 16 days. Chemical compositional analyses were performed at the positions marked with numbers from 1 to 15 in Fig. 7(a), (c), (f) and (h) and the results are summarized in Table 2. A major trend visible in both Fig. 7 and Table 2 is that HPT processing increases the solubilities of Sn and Pb in the Pb-rich and Sn-rich phases, respectively. For example, for the as-cast condition there is evidence for the presence of an Sn structure within the Pb-rich phase in Fig. 7(a) and (b). Nevertheless, the chemical composition analyses in Table 2 suggest spectrums 2 and 3 in Fig. 7(a) are pure Sn and most of the Sn-rich phases consist of pure Sn as indicated by spectrum 1. After HPT processing and storage at RT for 3 days, Fig. 7 (c) and (d) suggest the chemical composition is homogenous in this Pb-rich phase and the structure is FCC without the presence of the BCT structure of Sn in Fig. 7(e). Spectrum 7 shows there is 3.7 wt% Sn in this Pb-rich phase whereas the Sn-rich phase spectrum 6 indicates 1.6 wt% Pb in the Sn-rich phase. Thus, as self-annealing proceeds at RT, the solubility of Sn in the Pb-rich phase decreases significantly but the solubility of Pb in the Sn-rich phase decreases only slightly.

Spectra 9–11 from the centre to the edge of the Pb-rich phase in Fig. 7 (f) show a gradient increase of Sn content from 7.77 at.% to 22.4 at.% as documented in Table 2. This separating process is completed after 16 days of storage in the Pb-rich phase in Fig. 7(h) and (i) where structures with high Sn content such as spectra 13 and 14 in Table 2 have measured Sn contents of 97.11% and 85.65% respectively. Finally, Fig. 7(j) shows the HRTEM image of the boundary area of these structures with high Sn content and it is evident that these Sn structures have a BCT unit cell and a (111) plane lying parallel to the (001) plane of the Pb-rich phase which has an FCC unit cell.

The overall movement of the Pb-rich phase during self-annealing was monitored by *in situ* observations at the same location immediately after HPT after 2 and 7 days of storage at RT and the results are shown in Fig. 8(a–c) where the Pb-rich phase is shown in black. This movement may be modeled and illustrated as in Fig. 8(d–f). Specifically, there are two distinct and well-defined processes: in I on the left there is a pulling back of the stretched individual Pb-rich phase to the centre of each phase as indicated by the red arrows, and in II there is an agglomeration and the formation of large Pb phases as depicted schematically in Fig. 8(e–f) where the Pb-rich phases A and B in Fig. 8(b) join to form the Pb phase C in Fig. 8(c). It should be noted that both of these re-arrangement processes will result in an overall reduction in the surface area of the Pb-rich phase.

4. Discussion

4.1. Sixfold cyclic twinning in Sn

Sixfold cyclic twins of Sn are commonly observed in the solidification of SnAg, SnCu and SnAgCu melts in the form of solder balls [40,41]. This type of twinning often occurs with the same <100> rotation axis but on one of two different crystal planes, the {101} and the {301} planes which correspond to twin angles of 57.2° and 62.8°, respectively [26]. However, cyclic twins are generally not observed in pure Sn [40] and this is due to the nucleus of the sixfold cyclic twin which has a metastable/pseudo-hexagonal structure. In practice, the low symmetry in Sn necessitates a foreign atom in order to form a hexagonal unit cell at the core of the nucleus.

For bulk Sn alloys, there is very little information on the formation of cyclic twins. In Fig. 1, it was apparent that the Sn grains in each large domain fit into a 62.8°<100> twin relationship and thus the twinning plane is on the {301} plane. Therefore, it is reasonable to anticipate that in each domain there is one nucleation site with only one nucleus which is illustrated in Fig. 9. Thus, a Pb atom is required at the centre to form the hexagonal structure. The structure with two layers of atoms in Fig. 9 (a) should be replicated and rotated six times in order to form the nucleus in Fig. 9(b) but there is an obvious misfit caused by the angle of $\phi = 62.8°$ between the {301} planes in Fig. 9(a). This misfit may be accommodated through the existence of a large fraction of LAGBs as is evident for the as-cast sample in the histogram shown in Fig. 1(g).

For Sn alloys, when a critical solid nucleus forms during solidification, it grows sufficiently quickly that the surrounding environment heats up and this effectively suppresses other nucleation events. For example, a growth rate of 20 cm s^{-1} was measured for Sn with an undercooling of only 10 °C [42]. As a consequence, this leads to the formation of a limited number of Sn grains. This growth pattern with the formation of large dendritic arms is obvious for the 57.2°<100> twin

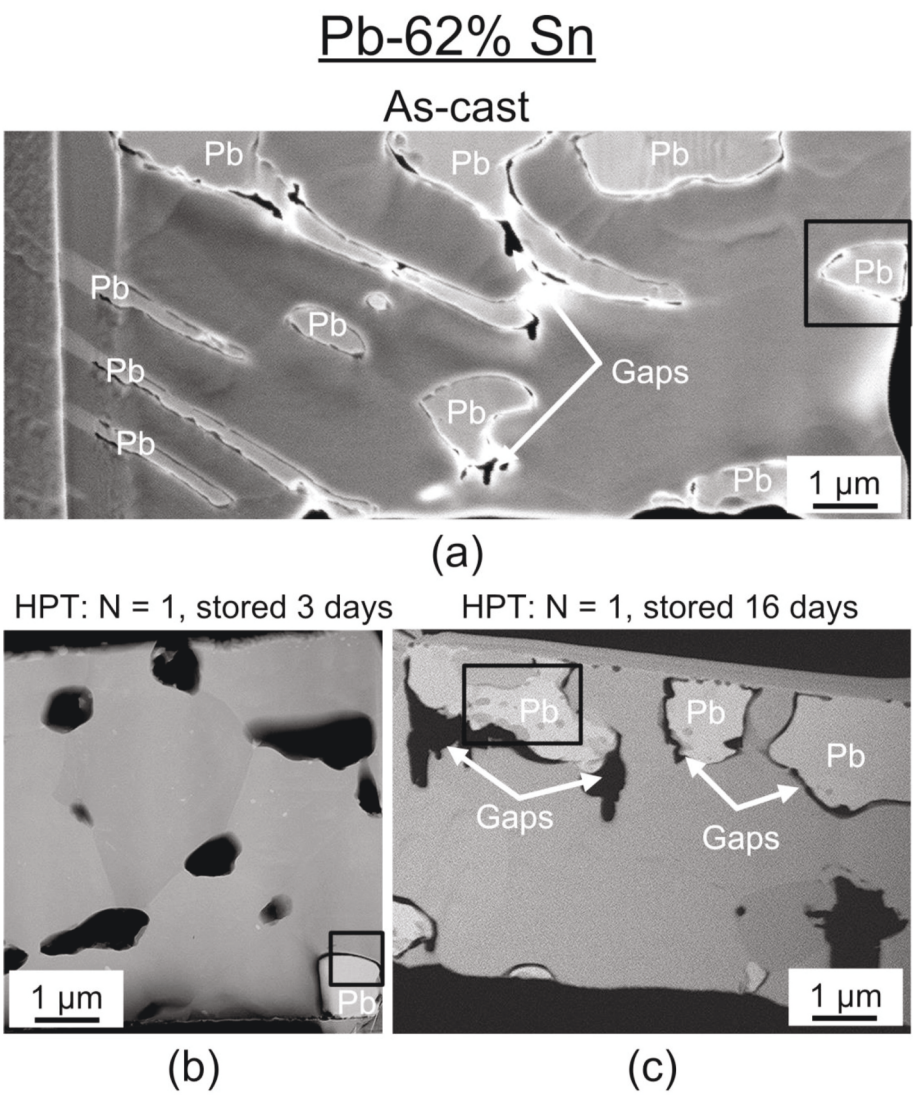

Fig. 6. SEM images of thin slices of samples (a) in the as-cast condition and after HPT processing for storing at RT for (b) 3 and (c) 16 days.

growth mode where the fast <110> and slow <001> growth directions of the nucleus fan outwards without interference. However, for the 62.8°<100> twins the situation is different. It is clear from Fig. 9(c) that the structure is faceted by {110} and {001} planes and these facet planes interfere with the growth direction as denoted by the arrows in Fig. 9(c). As a result, the nucleus in Fig. 9 should form a microstructure characterized by a large fraction of small dendrites from each twin segment interspersed on a cross-section with three dominant crystal orientations.

This type of microstructure is now well established and is generally termed "interlaced twins" [26]. Nevertheless, the numbers of nuclei are limited due to the large undercooling of Sn and therefore the domain size should be large as is evident from Fig. 1. Accordingly, it is difficult to measure a meaningful average grain size for microstructures with interlaced twins because many grains appear on the cross-sectional areas of each domain but these interlocked branch-like grains or dendrites are generally interconnected to three separate orientations which are formed from one nucleus. Thus, the limited numbers of orientations mean that each separate domain behaves more as a single large grain rather than as many small grains.

4.2. *The effect of pressure on grain boundary migration*

It is beneficial to firstly investigate the deformation mechanism of the Pb–Sn alloy by HPT before considering the nature of the grain boundary migration. The Pb–Sn alloy has a very low absolute melting temperature so that deformation at RT corresponds to warm deformation at a homologous temperature of $>0.4T_m$ and therefore it is reasonable to anticipate the occurrence of DRX during HPT processing [43]. The occurrence of DRX was confirmed in this investigation by the recrystallized microstructure with mostly equiaxed grains in Fig. 2(a) and (c). The advent of DRX often leads to a significantly finer grain size than in static recrystallization and thus the average grain size immediately after HPT is ~1.1 μm which is much finer than the value of ~2.5 μm for the initial as-cast sample. This means that the processing of the Pb–Sn eutectic alloy by HPT is accompanied by a recovery/recrystallization process where grain boundary migration occurs easily.

The imposition of a very high pressure in HPT has a significant influence on grain boundary migration and leads to the selection of certain types of grain boundaries for migration. For example, an early investigation showed the recovery process in heavily-deformed Al was significantly altered by a high pressure of 1.5 GPa at an annealing temperature of 553 K [29]. An investigation by TEM suggested a high fraction of the grain boundaries may be classified as high energy grain boundaries which are nominally HAGBs in low pressure annealing. This shows that the mobility of HAGBs is not affected by the high pressure whereas the migration of LAGBs appears to be limited [44]. The exceptionally low fraction of LAGBs of only 2%, corresponding to a sample examined immediately after HPT as shown in Fig. 4(a), is in excellent agreement

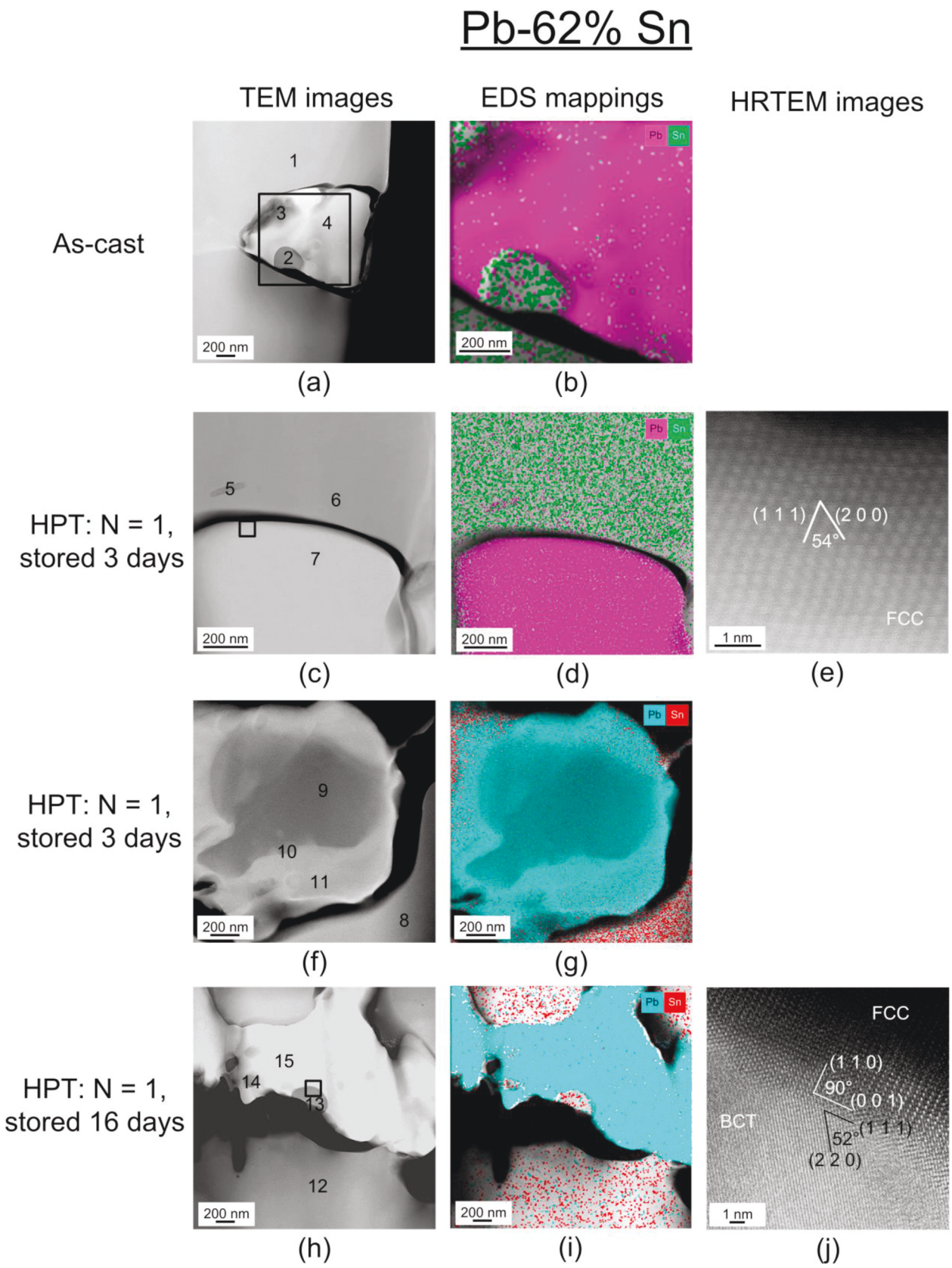

Fig. 7. TEM images (left column), EDS maps (centre column) and HRTEM images (right column) of an as-cast sample and a sample processed by HPT and stored at RT for 3 and 16 days.

Table 2
Concentration of Sn and Pb from the points marked 1–15 measured in Fig. 7

Spectrum	Sample state	Spectrum location	Pb (wt.%)	Sn (wt. %)	Pb (at. %)	Sn (at. %)
1	As-cast	Sn phase	0	100	0	100
2	As-cast	Vicinity of Pb phase	0	100	0	100
3	As-cast	Vicinity of Pb phase	0	100	0	100
4	As-cast	Pb phase	97.8	2.3	96.1	3.9
5	3 days	Sn phase	6.4	93.6	3.8	96.2
6	3 days	Sn phase	1.60	98.4	0.9	99.1
7	3 days	Pb phase	93.6	3.7	93.7	6.3
8	3 days	Sn phase	0.5	99.5	0.3	99.7
9	3 days	Pb phase	95.4	4.6	92.2	7.8
10	3 days	Pb phase	89.7	10.4	83.2	16.8
11	3 days	Vicinity of Pb phase	85.8	14.2	77.6	22.4
12	16 days	Sn phase	0.7	99.4	0.4	99.6
13	16 days	Vicinity of Pb phase	2.9	97.1	1.7	98.3
14	16 days	Vicinity of Pb phase	14.4	85.7	8.8	91.2
15	16 days	Pb phase	95.4	4.7	92.2	7.8

with these earlier results. When this sample is self-annealed at RT, the pressure is removed and the mobility of LAGBs is reactivated. Thus, the fraction of LAGBs increases to 11% after 11 days of storage under normal pressure as shown in Fig. 4(b). In addition, it is interesting to note that the numbers of random HAGBs which exclude special grain boundaries is low for the as-cast condition but increases after processing by HPT. This is demonstrated in Fig. 5 where the black curve for the as-cast condition is under 1% for random HAGBs since the peaks correspond to special grain boundaries whereas immediately after HPT processing the red line for 0 days lies at well over 1%.

For special grain boundaries, it is evident from Fig. 5 that the mobility of twin boundaries at 62.8° is greatly suppressed by the high pressure imposed during HPT whereas the mobility of the Σ21 boundaries at ~69–71° is favoured in the presence of this high pressure. When the sample is self-annealed at RT without application of a high pressure, the mobility of twin boundaries is reactivated and they start to actively migrate and consume some Σ21 boundaries, thereby causing a reduction in the fractions of these boundaries during storage. There are earlier reports of investigations on the mobility of special boundaries as well as random HAGBs in bicrystals of high purity Sn [29] and Al [30] under the presence of high pressure as the samples were annealed at elevated temperatures. In the investigation of high purity Al, it was demonstrated that the <110> tilt boundaries (Σ9, 36.9°<110>) appear to move by group transitions of atoms whereas the <100> and <111> tilt boundaries (Σ5, 36.9°<100> and Σ7, 38.2°<111>) appear to move by single atom transitions [30]. By contrast, the results for the high purity Sn suggested that group transitions are the dominant mechanism for both special boundaries and random HAGBs in the presence of a high pressure [29].

In practice, fewer atoms are involved in the migration of special grain boundaries in Sn bicrystals and the atomic volume is significantly lower than for random HAGBs. Thus, for Σ13 boundaries at 22.5° the numbers of atoms transited each time is $n = 20$ atoms and the atomic volume, V^*, is of the order of $\sim 0.24 \times 10^{-3}$ m^3/kg·atom whereas for random HAGBs at 25° there are $n = 28$ atoms transited each time and $V^* = 0.41 \times 10^{-3}$ m^3/kg·atom [29]. Therefore, based on the expression $\Delta V = nV^*$ which refers to the volume difference between the activated state and the ground state [45], the fact that special grain boundaries have lower activation volumes than random boundaries suggests the migration of special grain boundaries is energetically favoured in Sn in the presence of a high pressure. Although the earlier investigation on Sn bicrystals studied only Σ5, Σ13 and Σ17 boundaries, the results showed different values for n of 13, 20 and 21, respectively [29], so that the values of ΔV are different for the different special boundaries. Thus, the present investigation is consistent with a higher mobility of Σ21 compared with other special boundaries that may have smaller numbers of atoms in the presence of a high pressure.

4.3. The dislocation-twin boundaries

Another phenomenon observed in Fig. 3 is that the newly-formed grains have a near-twin relationship with the original grain but there is a slight deviation from the 62.8°<100> twin relationship. The presence of this deviation is further confirmed by the statistical grain boundary information shown in Fig. 5 where the twin boundary peak for

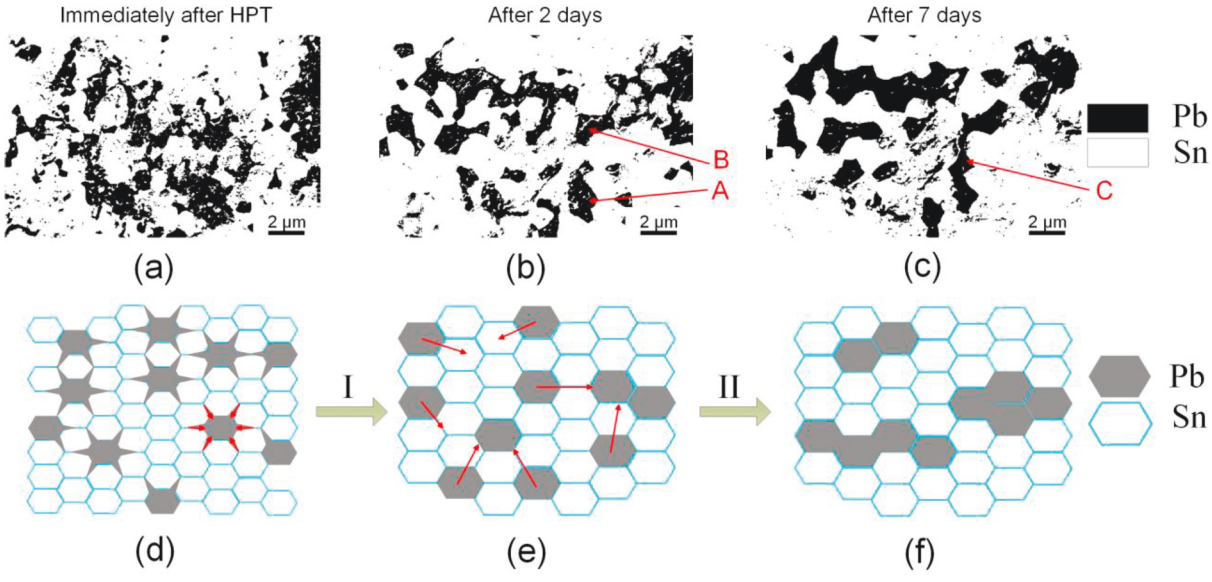

Fig. 8. In situ observations of Pb-rich phase during self-annealing after HPT processing: I shows the stretched Pb-rich phase pulled back to form spheroidal shapes and II shows the Pb-rich phase joining with near Pb phases to increase the size. These images are from SEM images where the Pb phase is extracted and assigned with black colour and the Sn phase is white and fills the remaining space. (For interpretation of the references to colour in this figure legend, the reader is referred to the Web version of this article.)

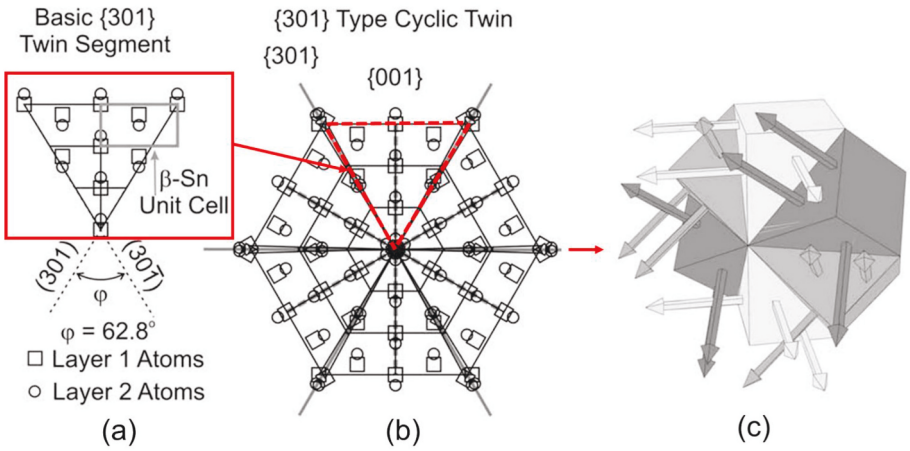

Fig. 9. A nucleus of a {301} sixfold cyclic twin: (a and b) projection views of the nucleus onto the (010) plane and (c) a construction of the twin nucleus faceted on {110} and {001} planes [26].

the as-cast sample lies exactly at 62.8° but for the HPT-processed samples after 2, 6 and 11 days of RT storage the peaks deviate slightly from the 62.8° twin relationship. These deviated twin boundaries may be explained from the theory of dislocation-twin boundaries [46–50] although many of these reports focus on HCP metals because twinning is then an important deformation mechanism.

In practice, an early report showed TEM images of dislocation-twin boundaries and a selected area electron diffraction pattern with a deviation of ~4° from the $\{10\bar{1}2\}\langle\bar{1}011\rangle$ twin relationship in a CP-Ti alloy processed by ECAP [50]. Another report showed similar dislocation twin boundaries with a deviation of 3.8° from the same twinning system in a commercial AZ91D magnesium alloy processed by surface mechanical attrition treatment (SMAT) which is also a form of heavy deformation [51]. It was concluded from these results that severe deformation produces a high density of dislocations and may thereby favour the formation of dislocation-twin boundaries. Consequently, when a slip dislocation meets a twin boundary, it may dissociate into interfacial defects such that these defects can aid twin growth if the dissociation products are sessile twinning dislocations and the stress state favours their motion in the twinning direction [52]. The formation of dislocation-twin boundaries occurs predominantly at the beginning of self-annealing and therefore immediately after processing by HPT when the density of dislocations is high. This is in agreement with the observation that twins with dislocation-twin boundaries having fast growth rates are visible during self-annealing in Figs. 2 and 3. Thus, the occurrence of a fast growth rate is explained by the favourable stress state which is caused by the dislocation-twin boundaries.

4.4. Solubility of Sn in the Pb-rich phase

At the eutectic temperature of 183 °C, the solubility limits of Sn in Pb and Pb in Sn are 19.2 wt% and 2.6 wt%, respectively. During cooling to RT, the Sn solubility in Pb decreases significantly to 1.3 ± 0.5 wt% whereas the Pb solubility in Sn reduces to only 0.3 wt% [53]. Thus, secondary Sn and Pb will precipitate from the original eutectic phases during solidification. Precipitates of both secondary Sn and Pb are visible in Fig. 7 where the Sn precipitate in the Pb-rich phase is marked as 2 in Fig. 7(a) and contains only Sn whereas the Pb precipitate in the Sn-rich phase is marked as 5 in Fig. 7(c) and contains 6.38 wt% of Pb.

It is readily evident that the precipitates dissolve after HPT in Fig. 7 (c–g) and the solubility of Sn in Pb is significantly increased by HPT. Additionally, the Pb solubility in Sn increases slightly to 1.6 wt% in spectrum 6 in Fig. 7(c). It should be noted that the Pb-rich phase remains as an FCC structure and the Sn precipitates remain as a BCT structure in Fig. 7(e) and (j) which suggests that the HPT has produced locally the formation of a supersaturated solution. This high solubility arises because processing by HPT generates a large number of defects including dislocations and vacancies [1] and all of these defects favour the dissolution of precipitates [54–56]. Furthermore, it was shown earlier that it is possible to produce extreme supersaturation through HPT as demonstrated in the processing of a metastable Al–Mg system [57,58]. Atomic mobility may be significantly promoted by HPT through grain boundary diffusion since the population of grain boundaries is high because the grain size is significantly refined by HPT [59] and a high dislocation density may also promote solubility through pipe diffusion and solute drag [60]. Nevertheless, the most likely mechanism in the present investigation is by the increase in the concentration of mobile vacancies which promotes the diffusion rate. It was reported earlier that the compressive strain and plastic deformation introduced by HPT will lower the vacancy formation energy and thereby promote the formation of excess vacancies [61–64]. Furthermore, under a compressive strain the vacancy migration energy may be lowered so that the vacancy mobility will increase [65].

Nevertheless, a supersaturated solution of the Pb-rich phase is not stable at RT. Thus, decomposition occurs after 13 days of storage as is evident in Fig. 7(h–j) where the Sn precipitates marked 13 and 14 form again in the vicinity of the Pb-rich phase. The lattice diffusion length, L, of the Sn atoms in Pb may be expressed as a function of time, t, through the relationship [66]:

$$L = 2\sqrt{D_{Sn}t} \tag{1}$$

where D_{Sn} is the lattice diffusion coefficient of element Sn which is 0.0085×10^{-14} m^2/s at 331 K (58 °C) [67]. Considering that the length of storage time from 3 to 13 days corresponds to 10 days or 1.1232×10^6 s, this gives a diffusion length of $L \approx 195$ nm at 331 K. The average widths of the areas with high concentrations of Sn in the Pb-rich phase shown in light grey in Fig. 7(f) and red dots in the EDS map in Fig. 7(d) are ~200 nm which is therefore within the range anticipated for lattice diffusion. Combining this information with the result in Fig. 7(h) where the Sn precipitates form again after 16 days of storage, it is reasonable to conclude that the decomposition and forming of the Sn precipitates in the Pb-rich phase during self-annealing occurs by lattice diffusion.

Finally, it should be noted that a re-agglomeration of the fine Pb-rich phase to a coarse phase is not likely to occur by lattice diffusion for two reasons. First, because the bonding between the Pb-rich phase and the Sn-rich phase is very weak as is clearly evident from the gaps visible in Fig. 6. Second, in Fig. 8(b) the Pb-rich phase A moves to a length of ~1 μm to bond with the Pb-rich phase B to form a larger Pb-rich phase C in Fig. 8(c) within a total time of 5 days. Now, according to Eq. (1) a storage time of 5 days should give a diffusion length at a temperature

higher than RT (331 K, 58 °C) of ~120 nm which is very much below the measured length. This demonstrates that it is more likely that the large-sized Pb-rich phase is deformed and stretched by the plastic deformation introduced by HPT and the surface area is therefore significantly increased. During storage, and in order to reduce the surface energy, the Pb-rich phase forms a more spheroidal shape in stage I and then re-joins a nearby Pb-phase as shown in stage II of Fig. 8. Thus, the Pb phase probably goes along the region boundaries where there is poor adhesion and sufficient space but nevertheless the exact mechanism requires a more detailed investigation.

5. Summary and conclusions

1. Measurements by EBSD on an as-cast Pb-62% Sn eutectic alloy suggest that the microstructure is divided into large domains with each representing a nucleus during solidification. Within each domain, there are three major orientations with a twin relationship of 62.8°<100> which is termed a sixfold cyclic twin. A large fraction of LAGBs is formed during solidification to accommodate the misfits of the sixfold cyclic twins.

2. Discs of the Pb–Sn alloy were processed by HPT for 1 turn at RT. It is demonstrated that the imposition of a high pressure has a significant effect on grain boundary migration. Specifically, there is very little mobility of LAGBs, the mobility of random HAGBs is not affected but the mobility of special grain boundaries of Σ21 at 71° is greatly favoured during processing by HPT. This is associated with a migration mechanism with fewer atoms transited each time and therefore a requirement for a lower activation volume in the presence of high pressure compared with other types of boundaries.

3. The migration of dislocation-twin boundaries near 62.8°<100> was observed to be favourable during self-annealing after the high pressure was removed. The stress state on the dislocation-twin boundaries was conducive to their migration and this explains the fast rate of grain growth for grains having these boundaries.

4. The solubility of Sn in the Pb-rich phase was significantly improved due to large numbers of mobile vacancies produced by the HPT processing so that a supersaturated state was formed immediately after HPT processing. Nevertheless, this supersaturated state was not stable at RT and decomposition occurred to separate Sn and Pb in the Pb-rich phase through the occurrence of lattice diffusion. The subsequent rejoining of Pb-rich phases during self-annealing appears to be associated with a reduction in surface energy rather than by lattice diffusion.

Data availability

The raw/processed data required to reproduce these findings cannot be shared at this time as the data also forms part of an ongoing study.

Credit author statement

Nian Xian Zhang: Investigation, Data curation, Writing – Original draft preparation
Megumi Kawasaki: Data curation, Reviewing and editing
Yi Huang: Data curation, Supervision, Reviewing and editing
Terence G. Langdon: Supervision, Reviewing and editing

Declaration of competing interest

The authors declare that they have no known competing financial interests or personal relationships that could have appeared to influence the work reported in this paper.

Acknowledgements

This work was supported in part by the European Research Council under ERC Grant Agreement No. 267464-SPDMETALS (NXZ, YH, TGL) and in part by the National Science Foundation of the United States under grant no. DMR-1810343 (MK).

References

[1] R.Z. Valiev, R.K. Islamgaliev, I.V. Alexandrov, Bulk nanostructured materials from severe plastic deformation, Prog. Mater. Sci. 45 (2000) 103–189.
[2] R.Z. Valiev, Y. Estrin, Z. Horita, T.G. Langdon, M.J. Zehetbauer, Y.T. Zhu, Producing bulk ultrafine-grained materials by severe plastic deformation, JOM 58 (4) (2006) 33–39.
[3] Y.T. Zhu, R.Z. Valiev, T.G. Langdon, N. Tsuji, K. Lu, Processing of nanostructured metals and alloys via plastic deformation, MRS Bull. 35 (2010) 977–981.
[4] T.G. Langdon, Twenty-five years of ultrafine-grained materials: achieving exceptional properties through grain refinement, Acta Mater. 61 (2013) 7035–7059.
[5] Y. Huang, T.G. Langdon, Advances in ultrafine-grained materials, Mater. Today 16 (2013) 85–93.
[6] R.Z. Valiev, T.G. Langdon, Principles of equal-channel angular pressing as a processing tool for grain refinement, Prog. Mater. Sci. 51 (2006) 881–981.
[7] A.P. Zhilyaev, T.G. Langdon, Using high-pressure torsion for metal processing: fundamentals and applications, Prog. Mater. Sci. 53 (2008) 893–979.
[8] A.P. Zhilyaev, B.-K. Kim, G.V. Nurislamova, M.D. Baró, J.A. Szpunar, T.G. Langdon, Orientation imaging microscopy of ultrafine-grained nickel, Scripta Mater. 46 (2002) 575–580.
[9] A.P. Zhilyaev, G.V. Nurislamova, B.-K. Kim, M.D. Baró, J.A. Szpunar, T.G. Langdon, Experimental parameters influencing grain refinement and microstructural evolution during high-pressure torsion, Acta Mater. 51 (2003) 753–765.
[10] J. Wongsa-Ngam, M. Kawasaki, T.G. Langdon, A comparison of microstructures and mechanical properties in a Cu-Zr alloy processed using different SPD techniques, J. Mater. Sci. 48 (2013) 4653–4660.
[11] L. Meng, J. Gao, Y. Zhong, Z. Wang, K. Chen, Z. Gao, Supergravity separation for recovering Pb and Sn from electronic waste, Separ. Purif. Technol. 191 (2018) 375–383.
[12] F. Moosakazemi, S. Ghassa, F. Soltani, M.R. Tavakoli Mohammadi, Regeneration of Sn-Pb solder from waste printed circuit boards: a hydrometallurgical approach to treating waste with waste, J. Hazard Mater. 385 (2020), 121589.
[13] L.C. Peixoto, A.D. Bortolozo, A. Garcia, W.R. Osório, Performance of new Pb-Bi alloys for Pb-acid battery applications: EIS and polarization study, J. Mater. Eng. Perform. 25 (2016) 2211–2221.
[14] Z. Bakour, A. Dakhouche, Electrochemical corrosion of Pb-Sn and Pb-Sb alloys for lead-acid battery applications, Acta Phys. Pol. A 134 (2018) 103–105.
[15] S. Kaur, A. Kaur, P.S. Singh, T. Singh, Scope of Pb-Sn binary alloys as gamma rays shielding material, Prog. Nucl. Energy 93 (2016) 277–286.
[16] S.K. Kang, A.K. Sarkhel, Lead (Pb)-free solders for electronic packaging, J. Electron. Mater. 23 (1994) 701–707.
[17] H. Tang, C. Basaran, Influence of microstructure coarsening on thermomechanical fatigue behavior of Pb/Sn eutectic solder joints, Intl J Damage Mechanics 10 (2001) 235–255.
[18] M.M.I. Ahmed, T.G. Langdon, Ductility of the superplastic Pb-Sn eutectic at room-temperature, J. Mater. Sci. Lett. 2 (1983) 59–62.
[19] M.M.I. Ahmed, T.G. Langdon, The effect of grain size on ductility in the superplastic Pb-Sn eutectic, J. Mater. Sci. Lett. 2 (1983) 337–340.
[20] E.A. El-Danaf, K.A. Khalil, M.S. Soliman, Effect of equal-channel angular pressing on superplastic behavior of eutectic Pb-Sn alloy, Mater. Des. 34 (2012) 235–241.
[21] M. Kawasaki, S. Lee, T.G. Langdon, Constructing a deformation mechanism map for a superplastic Pb-Sn alloy processed by equal-channel angular pressing, Scripta Mater. 61 (2009) 963–966.
[22] M.M.I. Ahmed, T.G. Langdon, Exceptional ductility in superplastic Pb-62 pct Sn eutectic, Metall Trans A 8A (1977) 1832–1833.
[23] D.W. Henderson, J.J. Woods, T.A. Gosselin, J. Bartelo, D.E. King, T.M. Korhonen, M.A. Korhonen, L.P. Lehman, E.J. Cotts, S.K. Kang, P. Lauro, D.Y. Shih, C. Goldsmith, K.J. Puttlitz, The microstructure of Sn in near-eutectic Sn-Ag-Cu alloy solder joints and its role in thermomechanical fatigue, J. Mater. Res. 19 (2004) 1608–1612.
[24] J. Gong, C. Liu, P.P. Conway, V.V. Silberschmidt, Formation of Sn dendrites and SnAg eutectics in a SnAgCu solder, Scripta Mater. 61 (2009) 682–685.
[25] T.R. Bieler, H. Jiang, L.P. Lehman, T. Kirkpatrick, E.J. Cotts, B. Nandagopal, Influence of Sn grain size and orientation on the thermomechanical response and reliability of Pb-free solder joints, IEEE Trans. Compon. Packag. Technol. 31 (2008) 370–381.
[26] L.P. Lehman, Y. Xing, T.R. Bieler, E.J. Cotts, Cyclic twin nucleation in tin-based solder alloys, Acta Mater. 58 (2010) 3546–3556.
[27] A.U. Telang, T.R. Bieler, A. Zamiri, F. Pourboghrat, Incremental recrystallization/grain growth driven by elastic strain energy release in a thermomechanically fatigued lead-free solder joint, Acta Mater. 55 (2007) 2265–2277.
[28] A. Alhamidi, K. Edalati, Z. Horita, S. Hirosawa, K. Matsuda, D. Terada, Softening by severe plastic deformation and hardening by annealing of aluminum-zinc alloy: significance of elemental and spinodal decompositions, Mater. Sci. Eng. 610 (2014) 17–27.
[29] D.A. Molodov, B.B. Straumal, L.S. Shvindlerman, The effect of pressure on migration of <001> tilt grain boundary in tin bicrystals, Scripta Metall. 18 (1984) 207–211.
[30] D.A. Molodov, J. Swiderski, G. Gottstein, W. Lojkowski, L.S. Shvindlerman, Effect of pressure on grain boundary migration in aluminum bicrystals, Acta Metall. 42 (1994) 3397–3407.

[31] N.X. Zhang, M. Kawasaki, Y. Huang, T.G. Langdon, The significance of self-annealing in two-phase alloys processed by high-pressure torsión, IOP Conf. Ser. Mater. Sci. Eng. 63 (2014), 012126.
[32] C.T. Wang, Y. He, T.G. Langdon, The significance of strain weakening and self-annealing in a superplastic Bi-Sn eutectic alloy processed by high-pressure torsion, Acta Mater. 185 (2020) 245–256.
[33] N.X. Zhang, M. Kawasaki, Y. Huang, T.G. Langdon, Microstructural evolution in two-phase alloys processed by high-pressure torsion, J. Mater. Sci. 48 (2013) 4582–4591.
[34] R.B. Figueiredo, P.R. Cetlin, T.G. Langdon, Using finite element modeling to examine the flow processes in quasi-constrained high-pressure torsion, Mater. Sci. Eng. 528 (2011) 8198–8204.
[35] R.B. Figueiredo, P.H.R. Pereira, M.T.P. Aguilar, P.R. Cetlin, T.G. Langdon, Using finite element modeling to examine the temperature distribution in quasi-constrained high-pressure torsion, Acta Mater. 60 (2012) 3190–3198.
[36] A.U. Telang, T.R. Bieler, The orientation imaging microscopy of lead-free Sn-Ag solder joints, JOM 57 (6) (2005) 44–49.
[37] M. Kawasaki, B. Ahn, T.G. Langdon, Microstructural evolution in a two-phase alloy processed by high-pressure torsion, Acta Mater. 58 (2010) 919–930.
[38] M. Kawasaki, B. Ahn, T.G. Langdon, Significance of strain reversals in a two-phase alloy processed by high-pressure torsion, Mater. Sci. Eng. 527 (2010) 7008–7016.
[39] T.-S. Cho, H.-J. Lee, B. Ahn, M. Kawasaki, T.G. Langdon, Microstructural evolution and mechanical properties in a Zn-Al eutectoid alloy processed by high-pressure torsion, Acta Mater. 72 (2014) 67–79.
[40] L.P. Lehman, S.N. Athavale, T.Z. Fullem, A.C. Giamis, R.K. Kinyanjui, M. Lowenstein, K. Mather, R. Patel, D. Rae, J. Wang, Y. Xing, L. Zavalij, P. Borgesen, E.J. Cotts, Growth of Sn and intermetallic compounds in Sn-Ag-Cu solder, J. Electron. Mater. 33 (2004) 1429–1439.
[41] P. Borgesen, T. Bieler, L.P. Lehman, E.J. Cotts, Pb-free solder: new materials considerations for microelectronics processing, MRS Bull. 32 (2007) 360–365.
[42] A. Rosenberg, W.C. Winegard, The rate of growth of dendrites in supercooled tin, Acta Metall. 2 (1954) 342–343.
[43] R.D. Doherty, D.A. Hughes, F.J. Humphreys, J.J. Jonas, D. Jensen, M.E. Kassner, W.E. King, T.R. McNelley, H.J. McQueen, A.D. Rollett, Current issues in recrystallization: a review, Mater. Sci. Eng. 238 (1997) 219–274.
[44] W. Łojkowski, J. Kwiecinski, J.W. Wyrzykowski, T. Łada, On the effect of high pressure on the grain boundary structures formed during recovery of aluminium, Defect Diffusion Forum 66–69 (1990) 957–960.
[45] G. Gottstein, D.A. Molodov, U. Czubayko, L.S. Shvindlerman, High-angle grain boundary migration in aluminium bicrystals, J. Phys. IV 5 (Colloque C3) (1995) C3-C89–C3-C106.
[46] P.G. Partridge, E. Roberts, The formation and behaviour of incoherent twin boundaries in hexagonal metals, Acta Metall. 12 (1964) 1205–1210.
[47] M.A. Gharghouri, G.C. Weatherly, J.D. Embury, The interaction of twins and precipitates in a Mg-7.7 at.% Al alloy, Philos. Mag. A 78 (1998) 1137–1149.
[48] X. Wu, N. Tao, Y. Hong, G. Liu, B. Xu, J. Lu, K. Lu, Strain-induced grain refinement of cobalt during surface mechanical attrition treatment, Acta Mater. 53 (2005) 681–691.
[49] Y.S. Li, N.R. Tao, K. Lu, Microstructural evolution and nanostructure formation in copper during dynamic plastic deformation at cryogenic temperatures, Acta Mater. 56 (2008) 230–241.
[50] Y. Zhang, Z.S. Dong, J.T. Wang, J.Q. Liu, N. Gao, T.G. Langdon, An analytical approach and experimental confirmation of dislocation-twin boundary interactions in titanium, J. Mater. Sci. 48 (2013) 4476–4483.
[51] H.Q. Sun, Y.-N. Shi, M.-X. Zhang, K. Lu, Plastic strain-induced grain refinement in the nanometer scale in a Mg alloy, Acta Mater. 55 (2007) 975–982.
[52] L. Capolungo, I.J. Beyerlein, C.N. Tome, Slip-assisted twin growth in hexagonal close-packed metals, Scripta Mater. 60 (2009) 32–35.
[53] M. Abtew, G. Selvaduray, Lead-free solders in microelectronics, Mater. Sci. Eng. R 27 (2000) 95–141.
[54] D.G. Morris, M.A. Muñoz-Morris, Microstructure of severely deformed Al-3Mg and its evolution during annealing, Acta Mater. 50 (2002) 4047–4060.
[55] M. Murayama, K. Hono, Z. Horita, Microstructural evolution in an Al-1.7 at%Cu alloy deformed by equal-channel angular pressing, Mater. Trans., JIM 40 (1999) 938–941.
[56] V.V. Sagaradze, V.A. Shabashov, Deformation-induced anomalous phase transformations in nanocrystalline FCC Fe-Ni based alloys, Nanostruct. Mater. 9 (1997) 681–684.
[57] J.-K. Han, K.-D. Liss, T.G. Langdon, M. Kawasaki, Synthesis of a bulk nanostructured metastable Al alloy with extreme supersaturation of Mg, Sci Rprts 9 (2019) 17186.
[58] J.-K. Han, K.-D. Liss, T.G. Langdon, J.-i. Jang, M. Kawasaki, Mechanical properties and structural stability of a bulk nanostructured metastable aluminum-magnesium system, Mater. Sci. Eng. A 796 (2020) 140050.
[59] B.B. Straumal, B. Baretzky, A.A. Mazilkin, F. Philipp, O.A. Kogtenkova, M. N. Volkov, R.Z. Valiev, Formation of nanograined structure and decomposition of supersaturated solid solution during high pressure torsion of Al-Zn and Al-Mg alloys, Acta Mater. 52 (2004) 4469–4478.
[60] D. Turnbull, R.E. Hoffman, The effect of relative crystal and boundary orientations on grain boundary diffusion rates, Acta Metall. 2 (1954) 419–426.
[61] X. Sauvage, F. Wetscher, P. Pareige, Mechanical alloying of Cu and Fe induced by severe plastic deformation of a Cu-Fe composite, Acta Mater. 52 (2005) 2127–2135.
[62] S.V. Divinski, G. Reglitz, H. Rösner, Y. Estrin, G. Wilde, Ultra-fast diffusion channels in pure Ni severely deformed by equal-channel angular pressing, Acta Mater. 59 (2011) 1974–1985.
[63] R. Wurschum, B. Oberdorfer, E.M. Steyskal, W. Sprengel, W. Puff, P. Pikart, C. Hugenschmidt, R. Pippan, Free volumes in bulk nanocrystalline metals studied by the complementarytechniques of positron annihilation and dilatometry, Physica B 407 (2012) 2670–2675.
[64] K. Oh-ishi, K. Edalati, H.S. Kim, K. Hono, Z. Horita, High-pressure torsion for enhanced atomic diffusion and promoting solid-state reactions in the aluminum–copper system, Acta Mater. 61 (2013) 3482–3489.
[65] B. Ahn, A.P. Zhilyaev, H.-J. Lee, M. Kawasaki, T.G. Langdon, Rapid synthesis of an extra hard metal matrix nanocomposite at ambient temperature, Mater. Sci. Eng. 635 (2015) 109–117.
[66] D. Gupta, K. Vieregge, W. Gust, Interface diffusion in eutectic Pb-Sn solder, Acta Mater. 47 (1998) 5–12.
[67] D.L. Decker, J.D. Weiss, H.B. Vanfleet, Diffusion of Sn in Pb to 30 kbar, Phys. Rev. B 16 (1977) 2392–2394.